Large Eddy Simulation of transitional flows in an elliptical finned-tube heat exchanger

Ephraïm Toubiana, Rémi Gautier, Daniel Bougeard, Serge Russeil

Version of Record: https://www.sciencedirect.com/science/article/pii/S1290072915303434
Manuscript_175256bd7c0201253a4a4c0a7a7c6a37

Large Eddy Simulation of transitional flows in an elliptical finned-tube heat exchanger

Ephraïm Toubiana[a,b], Rémi Gautier[a,b], Daniel Bougeard[a,b], Serge Russeil[a,b,*]

[a] *IMT Lille Douai, Institut Mines-Télécom, Energy Engineering Department, F-59508 Douai, France*
[b] *Université de Lille, F-59000 Lille, France*

Abstract

Three-dimensional numerical simulations of four rows elliptical finned-tube heat exchanger are performed within a Reynolds numbers range usually used in many applications including the laminar-turbulence transition. A highly-resolved Large Eddy Simulation (LES) approach is chosen in order to get reliable transition-to-turbulence data. This paper presents an analysis of the row-by-row evolution of flow topology and unsteadiness of the complex vortical structure throughout the heat exchanger for various Reynolds numbers. The simulations show several important unsteady and turbulence transition fluid flow features that impact heat transfer. It is found that the topology of the horseshoe vortex system is highly dependent on the row considered. Moreover the unsteadiness of the flow occurs sooner upstream from the trailing edge of the heat exchanger when the Reynolds number increases. At last an important increase of global Nusselt number value is correlated with the vortical turbulent structures and unsteadiness.

Keywords: Horseshoe vortex, LES, Finned-tube heat exchanger, Turbulence

*Corresponding author.
Email address: serge.russeil@mines-douai.fr (Serge Russeil)

1. Introduction

Finned-tube heat exchangers are widely used in several areas such as industrial, transportation, heating and air conditioning systems applications [1, 2]. Various geometrical configurations of finned-tube heat exchangers may be encountered. The tubes shape can be circular, elliptic or flat. Moreover, the tubes arrangement can be in-line or staggered. Due to its widespread utilization, this kind of heat exchangers has been extensively studied experimentally, see Tahseen et al. review [3] and even numerically using laminar [4] or Reynolds-averaged Navier-Stokes models [1]. The laminar-turbulent transition flow condition is commonly encountered in industrial applications of this kind of heat exchangers. However unsteady studies regarding laminar-turbulent transition flow over finned-tube heat exchangers are mainly limited to some unsteady Reynolds-averaged Navier-Stokes turbulence models, see for example Ref. [5].

Regarding the flow topology, several studies have shown that the tubes create a three-dimensional separation, due to adverse pressure gradient generated upstream which causes a reorganization of the boundary layer into a three-dimensional vortical structure called a horseshoe vortex system wrapping around the tube. As early shown by Baker et al. [6] in the case of a single tube mounted perpendicular to flat plate the horseshoe vortex system created is mainly composed of primary and secondary counter-rotating vortices which number, size and stability are linked to geometrical and flow parameters. Sahin et al. [7] investigated experimentally the characteristics of the turbulent flow field in the flow passage of a heat exchanger model comprised of two parallel plates and a cylinder located between the plates. They reported that the flow topology, the size of wake-flow region, the locations of singular points and values of turbulence quantities are strongly affected by the variation of the Reynolds number. Moreover they also studied the horseshoe vortex system in the passage of a plate-fin-and-tube heat exchanger model [8]. They analyzed how the vortices magnify the entrainment process which occurs between the main flow and the wake-flow regions and enhances the heat transfer rate. Simo Tala et al. [9] studied experimentally the flow characteristics in a multi-row plain fin-and-tube heat exchanger and highlighted that vortical system structure have both row-by-row and angular evolutions. Bougeard [10] showed that most of the heat transfer that occurs in the vicinity of the tube is strongly linked to the vortex juncture flow topology.

Nomenclature		
a	Semi- major axis of the tube section	(m)
b	Semi- minor axis of the tube section	(m)
F_p	Fin pitch	(m)
F_t	Fin thickness	(m)
P_t	Transversal tube pitch	(m)
P_l	Longitudinal tube pitch	(m)
x, y, z	Coordinates	(m)
u, v, w	Velocity components	$(m \cdot s^{-1})$
u', v', w'	Velocity fluctuations components	$(m \cdot s^{-1})$
u_τ	Wall friction velocity $\left(= \sqrt{\frac{\lvert\tau\rvert}{\rho}}\right)$	$(m \cdot s^{-1})$
u^+	Dimensionless velocity $(= u/u_\tau)$	$(-)$
y^+	Wall distance $(= u_\tau y/\nu)$	$(-)$
k	Turbulent kinetic energy per unit mass $\left(= \frac{\langle u'^2\rangle + \langle v'^2\rangle + \langle w'^2\rangle}{2}\right)$	$(J \cdot kg^{-1})$
$\Delta x^+, \Delta y^+, \Delta z^+$	Dimensionless grid spacing in x, y, z direction	$(-)$
D_h	Hydraulic diameter $(= 2 \cdot F_p)$	(m)
Nu	Nusselt number	$(-)$
Re_{2b}	Reynolds number based on minor axis $(= U_{in} \cdot 2 \cdot b/\nu)$	$(-)$
St_{2b}	Strouhal number $(= f \cdot 2b/U_{in})$	$(-)$
U_{in}	Inlet velocity (averaged)	$(m \cdot s^{-1})$
T	Temperature	(K)
τ	Wall shear stress	(Pa)
ρ	Density	$(kg \cdot m^{-3})$
q''	Heat flux density	$(W \cdot m^{-2})$
C_p	Specific heat	$(J \cdot kg^{-1} \cdot K^{-1})$
μ	Dynamic viscosity	$(Pa \cdot s)$
ν	Kinematic viscosity	$(m^2 \cdot s^{-1})$
λ	Thermal conductivity	$(W \cdot m^{-1} \cdot K^{-1})$
$\boldsymbol{u}$	Velocity vector	$(m \cdot s^{-1})$
$\boldsymbol{\omega}$	Vorticity vector	(s^{-1})
H	Helicity $(= \boldsymbol{u} \cdot \boldsymbol{\omega})$	$(m \cdot s^{-2})$
σ	Standard deviation	
Σ	Standard deviation divided by the mean value of a quantity	$(-)$
Subscript		
i, j, k	Vector component in x, y, z direction	
$tube$	Tubes	
in	Inlet	
out	Outlet	
Superscript		
$\langle\ \rangle$	Temporal averaging operator	
$\lvert\ \rvert$	Norm	
Abbreviation		
TKE	Turbulent Kinetic Energy	
LES	Large Eddy Simulation	
$RANS$	Reynolds-averaged Navier-Stokes	

Moreover, one of the important phenomenon that occurs when a fluid flows across multiple bluff bodies as in those kind of heat exchangers is the generation of a complex three-dimensional flow structure as a consequence of the mutual interactions among the wakes behind the bodies [11]. These wake interactions subsequently lead to some complex vortex shedding phenomena. Thus, the forced convection heat transfer and then the resulting thermal field are driven by this complex flow structure. Therefore, in order to improve the development of those heat exchangers it is essential to understand the vortex shedding mechanism.

As pointed out by Sahin et al. [7] the flow structures in separated flows or wake flows are extremely unsteady. Therefore flows of this type require spatial and temporal information of the entire flow fields to allow a quantitative detection of spatial structures. A significant proportion of publications even recent ones does not consider this phenomenon because the simulations are performed with a stationary model see [12, 13] for example. However, a few unsteady simulations carried out on different types of plate fin heat exchangers or tube banks heat exchangers show that the vortex shedding phenomena occur. Simo Tala et al. [5] studied with unsteady-RANS model the tube pattern effect on thermalhydraulic characteristics in a two-row finned-tube heat exchanger. They pointed out that vortex shedding appearing in the tubes wake under specific conditions. Delibra et al. [14] studied by unsteady-RANS model the flow through a matrix of round pins in staggered arrangement connecting heated walls of a plane channel. They underline that in contrast to LES, the unsteady-RANS shows some deficiencies in predicting the wakes behind pins, their structure, size and recirculation strength.

According to Kritikos et al. [15] the flow field development inside the heat exchanger core is being significantly affected by the main flow surrounding the tubes and an 'X-type' flow is developed. According to them, this type of flow that is surrounding the tubes and their wake regions, remain almost completely stabilized near the trailing edge region of the tubes. However, at the last row of tubes the development of the wake region is not being limited by the 'X-type' flow. This explains that a vortex shedding appears and the flow field develops an unsteady nature. Delibra et al. [14] explain the different behaviour in the last row by the fact that there are no downstream obstructions to feedback the pressure effects upstream.

Several authors have investigated unsteady flow in pin fin matrix geometries. Such matrix geometries are close to finned-tube heat exchanger geometries. The main differences occurs in the number of tubes rows (much larger

for pin fins) and channel height (fin pitch for finned-tube heat exchanger which represent a fraction of tube diameter for heat exchanger and several tube (pin) diameter for pin fin matrix). Such numerical investigations in pin fin matrix give insights of hydraulic phenomena that could occur in finned-tube heat exchanger and particularly regarding laminar-turbulent transition phenomena. Delibra et al. underline, that the flow around the first row, impinged by non-turbulent or low free-stream turbulence incoming flow, is laminar with possible separation-induced transition in the wake. That influences the flow structure and heat transfer to a large degree around the subsequent two to three pin rows. They add that further downstream, typically beyond the fifth pin row, for Re_{2b} numbers which correspond closely to those usually encountered in practical application, the flow is fully turbulent and almost periodic. Given those complex three-dimensional unsteady phenomena, with the turbulent transition problematic depending on the Reynolds some authors use more advanced simulations than stationary RANS. Delibra et al. [16] studied by means of unsteady RANS and by LES simulations the vortex structures and heat transfer in a wall-bounded pin matrix. They found that flow details reveals discrepancies, particularly around the first three pin rows, where the unsteadiness predicted by unsteady-RANS model shows much weaker amplitudes compared with LES. Then only further downstream, the successive series of pins produced unsteadiness which is captured with unsteady-RANS model similarly to those captured by LES. Regarding Large Eddy Simulations even if becoming more and more used, still very few simulations have been performed on finned-tube heat exchanger. Wen et al. [17] studied by Large Eddy Simulation the flow and heat transfer in a finned tube in direct air-cooled condensers. They also carried out a brief qualitative comparison between the LES and RANS simulations results. They found that unsteady flow fields in the wake region were predicted more precisely by LES method. They also estimated that LES calculations of transient fluid flow and heat transfer behavior, because they take into account wake interaction and vortex-shedding, provide a foundation for a better design of such heat exchangers.

Zhang et al. [20] studied unsteady behaviors of fluid flow and heat transfer in plain plate-fin and tube heat exchangers by a Large Eddy Simulation. Their study shows by using comparison with well-known experimental correlations, that LES has a better prediction of overall performance plate-fin and tube HX than RANS model. Moreover they point out that LES shows interesting unsteady phenomena of vortex shedding behind the tube. It is shown

that for small fin pitches the vortex shedding phenomenon development is avoided due to a confinement effect (viscous drag force from the two fins). For larger fin pitches vortex shedding phenomenon happens at dominant frequency close to bare tube bank. Unfortunately in their study, they assumed a symmetry plane on mid-plane (50% of the tube height) between two successive fins which is not a judicious choice in the framework of a Large Eddy Simulation. Even if this boundary condition can allow the development of vortex shedding phenomenon behind the tube it cannot simulate asymmetric vortex shedding in the vertical direction (along fin pitches), increasing the confinement effect. Baker [18] and Sahin [7] show experimentally that such unsteady vortex development occurs in front of the tubes in the horseshoe vortex system. The HSV system is found to be strongly unsteady for range of Reynolds number and for certain fin spacing. In other words the mid-plane symmetry of the horseshoe vortex system could be found only in time average. That is to say that a more rigourous way to capture all the unsteady phenomena that occur in platefin and tube geometry need to avoid the mid-plane assumption. In this article the midplane assumption is not retain to precisely simulate unsteady phenomena of HSV system and vortex shedding in tube wake.

Lai et al. [19] performed similar Large Eddy Simulation on plate-fin and tube heat exchangers with small diameter tubes. However in this case they assumed a symmetry plane in the span-wise direction which divide computational domain in the transverse direction to the half of transverse tube pitch. A serious weakness with this assumption, however, is that this symmetry condition does clearly not enable to predict the real instantaneous unsteady behaviour of the well-known vortex shedding phenomenon which is noted by many authors. Setting this symmetry on the topology of the instantaneous flow has a clear influence on the vortex shedding (inhibiting the growth) and also on the separation point on the tube. These two restrictive assumption are not made in the present paper.

Regarding the tube shape, some studies have shown that elliptic tube geometry has a better aerodynamic shape than the circular one [21, 22]. In fact, they lead to a lower pressure drop due to the smaller wake region on the fin behind the tube. Simo Tala et al. [5], also studied the effect of the tube shape modification (from circular to elliptic) on the air-side thermalhydraulic characteristics and entropy production rate using Unsteady-RANS simulations. They found an increase of thermal-hydraulic performance of above 80% with the reduction in the tube ellipticity compared with a circular shaped tube.

The purpose of this article is to study by Large Eddy Simulation a four rows elliptical finned-tube heat exchanger for four Reynolds numbers in the transitional regime with a particular focus on tubes aero-thermal characteristics. This study analyzes both the row-by-row evolution and Reynolds number influence of the complex three-dimensional vortical structure throughout the heat exchanger. Moreover in this study we use wall-resolved LES to characterize precisely the influence of turbulence spot and turbulence transition phenomena. An evaluation of the evolution of the unsteadiness, which is related to the transition to turbulence within the heat exchanger, and of its impact to the heat transfer rates is then performed.

2. Large Eddy Simulation

The Large Eddy Simulation (LES) methodology is used in this paper on a very fine mesh in order to ensure highly resolved simulations together with a subgrid model. This allows to accurately characterizing the unsteadiness and transition phenomena encountered in this kind of flow. This approach, by means of a filtering operation applied to the Navier-Stokes equations, resolves explicitly the dynamics of the unsteady large scales of turbulence while modeling the small scale motions.

Three-dimensional CFD calculations are carried out using the finite-volume-based CFD commercial code Starccm+ 10.02. In the present LES simulations, the Wall-Adapting Local Eddy-viscosity (WALE) [23] model is used for the modeling of the subgrid scale viscosity and a constant turbulent Prandtl number ($Pr_t = 0.9$) was employed. The WALE model is based on the square of the velocity gradient tensor and takes into account the effects of both strain and rotation rates to obtain the local eddy viscosity. It is specifically designed to return the correct wall-asymptotic y^{+3} behavior of the subgrid scale viscosity. For more accuracy a second order central differencing scheme is used for spatial discretization of the momentum equations. A second order formulation is also employed for temporal discretization and the physical time-step is carefully chosen for each simulation in order to produce a maximum local Courant number value of around 1, while the volume averaged Courant number is below 0.06 over the whole computational domain. Moreover regarding the fins, the heat diffusion equation is used to solve the temperature distribution.

The following assumptions are made:

- the working fluid is air with thermo-physical properties constant except for ρ (ideal gas law)

- natural convection and radiation are neglected

The thermo-physical properties of the air and the aluminum which are used for the heat exchanger fin are tabulated in Table 1.

Regarding the data provided by the simulations, before carrying out the data analysis, the achievement of statistical steady state was checked by monitoring the volume-averaged turbulent kinetic energy (time-averaged), and the pressure drop (temporal evolution). After waiting for the LES simulations to become statistically converged, the LES results are then statistically averaged for an additional time period of more than six flow-through times, while achieving a converged solution at each time-step [34].

2.1. Geometry and computational domain

A staggered fin-and-tube heat exchanger is studied in this paper. It is composed of four elliptical tube rows which ellipticity e is given by $e = a/b = 1.5$ (with a the semi-major axis and b the semi-minor axis). The computational domain of the elliptical finned-tube heat exchanger model studied is shown in Figure 1a. The fin pitch chosen is $F_p = 4.3mm$, the transversal pitch $P_t = 21mm$ and the longitudinal pitch $P_l = 20mm$ which are values typically encountered in such finned-tube heat exchangers.

The domain is, in the streamwise direction, extended to P_l upstream the heat exchanger and $5 \cdot P_l$ downstream in order to allow the boundary limit condition development on fin leading edge and to let the wake development downstream [24]. In the transversal directions the entire transversal pitch is considered in order to correctly take on consideration the vortex shedding and the entire fin pitch in order to correctly take on consideration the unsteady horseshoes vortices.

2.2. Boundary conditions

Boundary conditions are presented in Figure 1b. It is worth to note that for the problem considered in this paper, we focus on the transition throughout the heat exchanger, so regarding the incoming flow there is no periodicity in the flow direction. Therefore it is necessary to specify turbulence characteristics of the incoming flow at the inlet of the computational domain. The Synthetic Eddy Method (SEM) of Jarrin et al. (2006) [25] was chosen to

generate a turbulent inlet condition. This method is often used for engineering application see Ref [26, 27] for example. The inlet turbulence intensity I_{in} was set to 0.1 and the turbulent length scale was set to 0.3 mm which corresponds 7% of D_h [28, 29]. A constant inlet velocity is imposed with four Reynolds numbers $Re_b = 500,\ 1,000,\ 1,500,\ 2,500$ which corresponds respectively to $U_{in} = 1,\ 2,\ 3,\ 5\ m/s$. The air inlet bulk temperature is fixed to $T_{in} = 300K$ for all the simulations.

At the outlet of the heat exchanger the air pressure is fixed to the reference pressure $1.013 \cdot 10^5 Pa$. Moreover, tubes wall temperature are supposed constant $T_{tube} = 340K$. Heat conduction is taken into account in conductive fin (aluminium).

2.3. Mesh

Concerning the meshing issue, a fully hexahedral mesh is used for all the simulations. Regarding meshes spacing in wall units, the analysis of the wall distribution of y^+ shows that the condition of $y^+ < 1$ is achieved for all the simulations presented in the paper and the surface averaged y^+ value is less than 0.3. Moreover on core cells (out of the near-wall refinement zone) each cell is cubic, and grid size was chosen to ensure $x^+ < 18$ and $z^+ < 18$ which are more rigorous than usual recommendations for LES calculations, see Piomelli et al. [30] for example. Furthermore to quantify the quality of the mesh resolution, in an a posteriorly check, the volume of the cells V were compared to the Kolmogorov scale $\eta = \left(\frac{\nu^3}{\epsilon}\right)^{1/4}$. To that aim the ratio $V^{1/3}/\eta$, which represents the ratio between the cell size and the Kolmogorov scale was estimated by using the time-averaged energy dissipation rate within each cell $\epsilon = \epsilon_{res} + \epsilon_{SGS}$, where ϵ_{res} is the resolved dissipation rate and ϵ_{SGS} the modeled dissipation rate. For all the simulations performed and presented in this paper this ratio was found below 10 over the whole domain ensuring very precise estimation of turbulent quantity. This very fine grid, in the entire computational domain and not only in near walls region, is an important feature. Indeed as shown by Ref. [31], the motions responsible for the dissipation of turbulent kinetic energy are in the range of 8 to 60 times the Kolmogorov length scale, with a peak of the dissipation at about 24. Thus, considering the ratios that we obtain, the grid density used in the present simulations is undoubtedly capable of solving a large part of the dissipation spectrum and ensuring a good prediction of transitional flow. As an indication, a grid of approximately $6 \cdot 10^6$ cells is used in order to get those

well-resolved LES.

2.4. Numerical model validation

To validate the accuracy of the present LES solver the simulation of a flat plate channel flow is performed and compared with Moser et al. [32] DNS data for friction Reynolds number $Re_\tau = 180$. The mesh resolution is similar to that one adopted for LES simulations performed in our geometry and same choices about the numerical model (second order) as well as same analysis procedure. As it can be observed on Figure 2 the present LES results fit very well with the reference DNS data for the the production of turbulent kinetic energy (2a) as well as for the first component of the Reynolds stress tensor (2b).

3. Results and discussion

The results presented here under are divided into three paragraphs. The first paragraph gives a brief overview and analysis of the flow and heat transfer characteristics for a basic case of tube-fin junction flow which characteristics remain mainly steady and laminar to introduce the phenomena and terminology. Then it is followed by a second paragraph which analyzes the influence of the tube's row number on the flow and heat transfer characteristics. In the third and main paragraph, the Reynolds number influence on instabilities and turbulent structures formation are investigated.

The Nusselt number used in the following paragraphs is defined as follows:

$$Nu = \frac{q" \cdot D_h}{\Delta T_{lm} \cdot \lambda} \tag{1}$$

with

$$\Delta T_{lm} = \frac{(T_{tube} - T_{in}) - (T_{tube} - T_{out})}{ln[(T_{tube} - T_{in})/(T_{tube} - T_{out})]} \tag{2}$$

and $q"$ the local instantaneous wall heat flux density.

3.1. Basic case analysis: first tube row at $Re_{2b} = 500$

As mention earlier, in the vicinity of each fin/tube junction, several vortical structures may develop due to adverse pressure gradients. The resulting horseshoe vortical systems is then composed of several counter-rotating vortices which interact with the fins and tubes walls. In order to introduce this basic flow topology and the corresponding usual terminology, Figure 3

presents an illustration of such typical horseshoe vortical structures encountered upstream a tube in the plane of symmetry of the tube perpendicular to the fin. We can observe in particular the vortices named primary vortices, secondary vortices and corner vortex. Figure 4 show the vortical structures together with the corresponding wall Nusselt distribution on the fin and tubes wall in order to demonstrate their strong relation. The vortical structures are highlighted by the vortical Q-criterion [33] and by the helicity $H = \boldsymbol{u} \cdot \boldsymbol{\omega}$ (with $\boldsymbol{u}$ the velocity vector and $\boldsymbol{\omega}$ the vorticity vector) in several successive radial planes around the tubes. For the case presented in this figure we can find only a single primary vortex and a corner vortex at each fin/tube junction. It can be observed for $\theta = 0°$ (plane of normal y-axis upstream the tube, see figure 1c for the definition of θ) a single primary vortex at each junction (top/bottom fins). For increasing θ angle, it can be noticed that, in the very near tube area, a counter rotating corner vortex appears and develops as the primary vortex disappears. Regarding the Nusselt wall distribution, a U-shape zone of local maximum value of Nu wrapping around the tube can be noticed on the fins, see letter m_1 on figure 4. It corresponds to the primary horseshoe vortex imprint. Moreover, on the tube surface, there is also an area of local maximum Nu values on upstream part of the tube, see letter m_2, which is also directly linked to the primary horseshoe vortex. To analyze more deeply the impact of those vortices on the tube wall, the z-component of the wall shear stress (τ_k) on the tube is presented in Figure 5 as well as two radial planes ($\theta = 0°$ and $\theta = 90°$) with tangential velocity vectors to highlight the flow direction. The red color represents positive value of τ_k whereas negative values are represented by the blue color. As shown on this figure, the z-component of the wall shear stress (τ_k) allows to identify the influence of the near-wall horseshoe vortices on the tubes. Moreover we note that this figure can be linked with Figure 4. A negative value of τ_k is directly linked to a positive value of the helicity and vice versa. First of all it can be noticed that several counter-rotative vortices are present on the tube near-wall area. Between each near-wall counter-rotative vortices, we notice on the tube wall a zone where $\tau_k = 0$ (in the junction between $\tau_k > 0$ and $\tau_k < 0$, zones colored by grey color). In this zone, the tangential velocity vector is normal to the wall. We refer to an upwash region if velocity vectors are upward-directed and to a downwash region if velocity vectors are downward-directed towards the tube wall. As it will be discussed further in the next paragraphs, the configuration of the flow between two counter-rotative vortices has an impact on heat transfer. Upstream the tube for small angle θ, the downwash zone,

is identified by the D_1 letter. This zone is located between the two primary horseshoe vortices developing upstream. When the θ angle increases from the stagnation point ($\theta = 0°$), this zone become an upwash zone, identified in the figure by the letter U_1. This upwash zone that is located between a pair of counter-rotative vortices (corresponds to corner vortices) which have respectively an inverse direction of rotation from the main primary vortices that they follow. In addition, the corner vortex development with θ angle from the fin/tube junction for $\theta = 0°$ lead to another upwash zone identified in the figure by the letter U_2. Those observations explain the high value of Nu distribution observed in Figure 4 in the mid-plane area. In fact, in the downwash zone the velocity configuration lead to the bringing of cold fluid toward the hot tubes which leads to an increase of the heat exchange. Thus we observe that the heat transfer on both the tubes and plate-fins is strongly related to the surrounding flow structure and configuration.

3.2. Row impact: row by row evolution for $Re_{2b} = 500$

After the presentation, on a basic case, of the flow developing at a fin/tube junction, the row by row evolution is analyzed here for the four rows heat exchanger and for one value of the Reynolds number ($Re_{2b} = 500$). The other simulations for the other Reynolds numbers will be discussed in the following section.

To analyze the flow impact on the tubes near-wall area the z-component of the time-averaged wall shear stress τ_k distribution are reported on Figure 6a. Two kinds of topology behavior can be identified. The first one corresponds to the two first rows of tubes (R_1 and R_2) and the second one corresponds to the two other ones (R_3 and R_4). For the two first rows of tubes, the topology had been already described on the basic case. For the two last tubes rows, the distribution of τ_k is quite different. On half-height of the tube there is an upwash zone since $\theta = 0°$ (instead of the downwash zone identified on the same location for the two first rows), which is identified by U_1' on the figure. Moreover there is still downwash zones, see D_1' zone on the figure. Those downwash zones are not located in the half-height of the tube but on both sides of it.

Regarding the heat transfer the local time-averaged Nusselt number $\langle Nu \rangle$ distribution on the heat exchanger is presented on Figure 7a. First of all we can observe that $\langle Nu \rangle$ is globally higher for the two first rows. Moreover $\langle Nu \rangle$ has a low value on each tubes wake. Furthermore we can also distinguish imprints of the horseshoe vortex system on fin $\langle Nu \rangle$ distribution, see letters

M_2, M_3 and M_5' on the figure. For the two first tube rows, it can be observed a high value of $\langle Nu \rangle$ close to the half-height zone for small θ angle values, see letter M_2 on Figure 7a, which corresponds to the downwash zone (see D_1 letter on Figure 6a). On the contrary for the two last rows, it can be found a local minimum value of $\langle Nu \rangle$ near to the half-height for small value of θ angle, which corresponds to upwash zone (see U_1 letter on Figure 6a). Moreover, the local maximum value of $\langle Nu \rangle$ highlighted on the figure by the letter M_4 corresponds to the downwash zone observed on Figure 6a, letter D_1'.

Regarding the angular evolution of the heat exchange over the tubes, similarly to the flow structure, we can also decompose the four tubes into two part: the two inlet tubes (two first rows) and the other rows. For the two inlet tubes it can be noticed that the maximum value of $\langle Nu \rangle$ is reached for $\theta = 0°$ (stagnation line), and with the increase of θ there is an important decrease of $\langle Nu \rangle$ until $\theta = 158°$ (value taken from results analysis not explained in details) for the first row and $\theta = 150°$ for the second row. Then there is a very slight increases of $\langle Nu \rangle$ with θ, where $\langle Nu \rangle$ value nevertheless remains low. For the two other rows, the behaviour of $\langle Nu \rangle$ according to θ is quite different. In fact, the maximum value of $\langle Nu \rangle$ is not located near to $\theta = 0°$ ($\theta = 32°$ for R_3 and $\theta = 34°$ for R_4). Moreover this maximum value is significantly below the maximum value of $\langle Nu \rangle$ for R_1 and R_2. This can be explained by the fact that R_3 and R_4 tubes are located in the wake of respectively R_1 and R_2 tubes. This is due to that around $\theta = 0°$ area (upstream face) the impinging velocity is significantly lower than in the same area for R_1 and R_2 as it can be observed in Figure 10a which is further discussed later. Then the trend is similar to R_1 and R_2 when θ increases, there is an important decrease of $\langle Nu \rangle$ with a minimum value at $\theta = 152°$ for R_3 and at $\theta = 132°$ for R_4. The minimum values of $\langle Nu \rangle$ are located in the recirculation zone and a low value area of the velocity.

Moreover it is interesting to note that the maximum value of $\langle Nu \rangle$ has been reached by the second row's tube. This could be explained by the velocity increase around the tube, in comparison to the first row tube, see Figure 10a. Furthermore the stronger primary horseshoe vortex in the second tube row lead to the higher peak of $\langle Nu \rangle$ in this zone.

3.3. Reynolds influence and unsteadiness

The aim of this paragraph is to examine qualitatively the Reynolds number influence on the flow structure and instabilities, and on the heat transfer

throughout the heat exchanger. To this purpose, four Re_{2b} are analyzed here: $Re_{2b} = 500/1,000/1,500/2,500$ which include the laminar-turbulence transition, where RANS models are particularly not reputed to be accurate [34]. The present LES simulations allow identifying precisely the evolution of the unsteadiness according to each row for each Reynolds number.

3.3.1. Flow topology and turbulence

Regarding the Reynolds number impact on flow topology near tubes walls, Figure 6 compare the z-component of the time-averaged wall shear stress τ_k distribution. It can be noticed that compared to the basic Reynolds number $Re_{2b} = 500$, when Re_{2b} increase ($Re_{2b} \geq 1,500$), the near-wall vortices which are revealed by τ_k are quite similar. However, for the two last tubes rows, a new pair of counter-rotative vortices appears. This leads to a downwash zone, identified by D_2 on Figure 6b and 6c which follows the U_1' upwash zone and a new significant upwash zone, identified by U_3.

In figure 8, the λ_2 vortex criterion [35] is used to identify instantaneous vortical structures in the flow passage for three of the Reynold numbers studied here. Those vortical structures are colored by the time-averaged turbulent kinetic energy (TKE) with a logarithmic scale. Moreover, in order to quantify the transition to turbulence inside the heat exchanger, the row-by-row volume averaged and time averaged TKE k (normalized with the kinetic energy associated with the inlet velocity $U_{in}^2/2$) is shown on Figure 9 in both linear (9a) and logarithmic scales (9b). The considered volume for the calculation of each row corresponds to the longitudinal tube pitch (see the area highlighted by red dotted line for the second tube row in Figure 1c).

We observe inside the heat exchanger flow passage that for $Re_{2b} = 500$, U-shaped vortical structures are symmetrically distributed around each fin-tube junction. These vortical structures correspond to the horseshoe vortical systems that are, for this Reynolds number, steady. Indeed, inside the heat exchanger, the averaged value of normalized TKE (figure 9b) remains at low values ($k/(U_{in}^2/2) < 0.01\%$) for $Re_{2b} = 500$. For $Re_{2b} = 1000$ the normalized TKE remains low ($< 0.01\%$) but a significant increase (more than one order of magnitude) is observed from the first row ($\approx 0.01\%$) to the last row ($\approx 0.2\%$). This indicates that, for $Re_{2b} \leq 1,000$, the horseshoe vortex system is more and more unsteady as both the Reynolds number and tube row increase, even if the regime remains laminar inside the heat exchanger. However, for both $Re_{2b} = 500$ and $Re_{2b} = 1,000$, downstream the heat exchanger, Von Karman-like asymmetric vortex shedding is found which shows

the unsteadiness of the flow. In this area the flow is significantly more turbulent than in the heat exchanger even if values remain lower than for other Reynolds numbers. $Re_{2b} = 1,500$ can be viewed as the start of the transition to turbulence inside the heat exchanger. We notice around the fourth tube some asymmetric turbulent vortical structures in addition to unsteady horseshoe vortices. Those vortical structures are responsible to the increase of TKE (figure 9a) in the vicinity of the fourth tube row ($k/(U_{in}^2/2) \approx 5\%$), while more than two order of magnitude of TKE is found between the first ($\approx 0.02\%$) and the fourth tube (figure 9b). It can also be noticed than the normalized TKE reaches approximately 1% for the third tube. Downstream the heat exchanger, the vortex shedding is more three dimensional with a wider range of vortex scale and the maximum value of TKE is closer to the last tube of the heat exchanger. For $Re_{2b} = 2,500$, it is interesting to note that the instantaneous turbulent structures are observed already around the third tube (figure 8), and lead to a global increase of the TKE which reach 6% in this area (figure 9a). Fully turbulent regime is found around the fourth tube row where the TKE increases up to nearly 20% of the inlet kinetic energy. Thus, with the increase of Re_{2b}, the unsteadiness, which is developing downstream the heat exchanger from the last row, moves toward opposite direction to the flow direction and inner tubes are more impacted as TKE globally increases within the heat exchanger. The increase of turbulent intensity for the second tubes row is then expected for higher flow regimes ($Re_{2b} > 2500$).

To further illustrate this evolution, Figure 10 shows the instantaneous velocity magnitude in the mid-plane in-between the fins for the same three Reynolds numbers. The influence of the evolution of the turbulence according to the tube rank and Re_{2b} on the velocity field can be observed. Indeed, we notice that for $Re_{2b} = 500$, downstream each tube the wake zone is characterized by very low values of velocity. For the fourth tube this zone extends over a relative large distance until the vortex shedding starts to develop. The reason lies in the fact that the last tube wake region is not being confined by the 'X-type flow' (confinement effect due to staggered tubes rows) as this was named by Kritikos [15]. However when the turbulence increases with the increase of Re_{2b}, this low velocity area downstream the fourth tube decreases and almost disappears for $Re_{2b} = 1,500$. Similarly, for $Re_{2b} = 2,500$, downstream the third tube, this low velocity zone is significantly reduced with a more important homogenization of the velocity value.

The laminar to turbulence variation can also be assessed by analyzing

the row-by-row unsteadiness which can be characterized by the local variation of velocity's y-component v at several locations within the heat exchanger. Here, the adimensional parameter Σ_v, the standard deviation σ_v divided by the time-averaged value $\langle v \rangle$, is considered. The probes are located on the mid-plane inbetween the fins, upstream (named P_{U1} to P_{U4}) and downstream each tube (named P_{D1} to P_{D4}), see Figure 1c. Figure 11a shows the row-by-row evolution of Σ_v for $Re_{2b} = 2500$ and highlights the difference of unsteadiness between upstream and downstream of each tube. Results for the other Reynolds numbers are quite similar: the maximum values is located downstream the last row and weaker values are found for the other tube rows. Moreover, for all Reynolds numbers and for each row of tubes, the upstream values (P_{Ui}) of Σ_v are always greater than the downstream ones (P_{Di}). Then, it is important to point out that the row-by-row volume-averaged of TKE plotted in Figure 9 mainly depends on fluctuations occuring in the near wake of each tube. This remark has been confirmed by the temporal capture of λ_2 criterion where the unsteadiness of the horseshoe vortices is clearly higher downstream than in the front of the tube. A video presenting the time-evolution of instantaneous turbulent structures can also be seen in appendix.

A detailed spectral analysis has been done on velocity y-component v for all tube row at different P_{Ui} and P_{Di} locations. This analysis shows that the unsteadiness can be characterized by one or multiple peaks with various amplitudes depending on tube row and flow regime. Figure 11b shows the power spectral density of velocity y-component v downstream of the fourth tube (P_{D4}) at $Re_{2b} = 2500$. A distinct peak is found at $St_{2b} = 0.32$. This peak is typical of such configuration of plate fin heat exchanger that produces vortex shedding phenomenon downstream the last tube row, as previously reported by Zhang et al.[20] on a similar heat exchanger configuration that the present paper. Moreover, classical turbulence decay of inertial frequencies at the slope of "-5/3" is also observed for more than one decade downstream the heat exchanger showing that the energy transfer from the largest to the smallest turbulence scales is well ensured by the subgrid scale model.

In order to understand the vortex shedding phenomenon inside the plate-fin heat exchanger and its attenuation by the damping phenomenon due to ducting effect, we present on Figure 11c the presence of the two dominant Strouhal numbers (corresponding of peaks of significant amplitudes) for $Re_{2b} = 1500$ and $Re_{2b} = 2500$. On this figure, Reynolds and Strouhal numbers are based on inlet (or bulk) velocity U_{in} and the tube diameter (val-

ues from literature were converted if needed). Results from previous articles [37, 38] are shown as well, where vortex shedding phenomenon in tube bundles were studied. For this configuration, results from [37, 38] shows clearly that specific Strouhal number of $St_D = 0.35$ is found associated with a secondary frequency [37], in that kind of configuration with no fin confinement effect (tube bundle). For plate-fin configuration Zhang et al. [20] reported also the same value outside the coil (after the fourth tube row). Hence, our study confirms the presence of a vortex shedding with $St_{2b} = 0.35$ at the last row of tube showing clearly that the confinement effect does not have any influence on the unsteadiness downstream the last row of tubes (i.e. outside the coil).

The present analysis of unsteadiness for each tube row also confirms on Figure 11c that the fin pitch has a major influence on dominant and secondary frequencies occuring downstream the first three rows inside the coil. In the present study where fin pitch is $F_p = 0.54D$, a primary peak is observed at $St_{2b} = 0.73$ at the third row and a secondary peak is also found at $St_{2b} = 0.49$. For tube bundle (without confinement effect) [37] also reported the Strouhal value of $St_D = 0.49$ as the secondary peak. In the case of confinement effect, but with higher fin pitch than ours (i.e. lower confinement effect), [20] found also this value as the primary peak for the third tube row. Hence, our results tend to confirm the result of Zhang et al. [20] claiming that vortex shedding phenomenon development is avoided due to the confinement effect depending on fin pitches values (see introduction of present article).

The present LES also detected the birth of unsteadiness at the first two rows with very low normalized TKE values (lower than 1%) without the presence of a clear vortex shedding phenomenon (as seen in video and in figure 8). As the tube row increases, there is a drastic increase of turbulence intensity (figure 9) where the vortex shedding phenomena occurs.

3.3.2. Heat transfer

In Figure 7 the time-averaged distribution of the Nusselt number Nu on fin and tubes wall is presented for $Re_{2b} = 500$ (already analyzed in the previous section) and $Re_{2b} = 2,500$. For $Re_{2b} = 500$ very low $\langle Nu \rangle$ values zones are observed downstream each tube. Those zones correspond to the recirculation zones and low values of the velocity. However we can clearly observe that for $Re_{2b} = 2,500$ downstream the third tube row, this relative low $\langle Nu \rangle$ values zone is significantly reduced due to the turbulent unsteady structures. Furthermore downstream the last tube row the zone of low $\langle Nu \rangle$

values completely disappeared, see letter M_6 on Figure 7b. We also note that for the last tube row, the value of $\langle Nu \rangle$ for $\theta \geq 104°$ increases significantly with a mean (z-direction averaged) maximal value of about $\langle Nu \rangle = 33$ for $\theta = 180°$ which is about eight time higher than for the first row. In fact the augmentation of the instabilities leads to a better mixing of the flow downstream the time-averaged separation point, and then it brings cold fluid toward the hot fin and tubes wall. In addition, backward facing downstream part of tube is impacted by backflow coming from outside of heat exchanger [36]. Moreover, we can note that for $Re_{2b} = 2,500$, unlike for $Re_{2b} = 500$, the value of $\langle Nu \rangle$ for $\theta = 0°$ of the two last tube rows is of the same order of magnitude of two first ones. This means that the turbulence increase reduces the impact of the two first tube rows wake on the two last tube rows leading edge.

We can also notice that the impact of the horseshoe vortices on fin's time-averaged Nusselt number distribution is clearly visible with a significant increase noticed at each fin-tube junction. In particular on downwash zones between two counter-rotative horseshoe vortices, see the zone identified by M_1 letter. The impact of those tubes near-wall counter-rotative vortices for each value of Re_{2b} are clearly observable on Nu distribution, see letters M_2 and M_4 on Figure 7b for $Re_{2b} = 2,500$. Thus the sequence of upwash-downwash zones due to the counter-rotative vortices systems which leads to sequences of increases and decreases of $\langle Nu \rangle$ highlights the variety of vortices on the plate-fin and tube $\langle Nu \rangle$ distribution.

In order to analyze quantitatively the impact of the vortices and instability on the heat exchanger, we present firstly in Figure 12a the time-averaged mean value of the Nusselt number on each tube wall according to the row number. We note that, there is an increase between the first and the second tube, then a significant decrease between the second and the third row and then again an increase between the third and the last row. Moreover it is interesting to note that the highest time-averaged mean value of Nu is located on the second-row for the two lower values of Re_{2b} whereas for the highest value of Re_{2b} it is located on the last row. This shows the impact of the increase of turbulence on the last tubes row.

Secondly, in order to evaluate the impact of the flow unsteadiness on the global fluctuations of the heat exchange, Figure 12b presents the value of the standard deviation divided by the time-averaged of the surface averaged Nusselt number $\Sigma_{Nu} = \sigma_{Nu}/\langle Nu \rangle$ over each tube. It is found that for $Re_{2b} = 500$, the value of Σ_{Nu} is almost constant according to the tube row, with a very

low value i.e. $\Sigma_{Nu} = 0.6\%$. Thus the instabilities of the tubes Nusselt number are negligible whatever the row position. For $Re_{2b} = 1,000$ though that Σ_{Nu} has a low value for each tube's row, it can be observed a slight increase of Σ_{Nu} for the two last rows which reflects an increase of Nu unsteadiness. For $Re_{2b} = 1,500$ the increase of Σ_{Nu} for the two last rows is even more significant with $\Sigma_{Nu} = 1.5\%$ for the last tube row. Finally, for $Re_{2b} = 2,500$, the value of Σ_{Nu} reaches about 2% for the third tube and nearly 5% for the last row. Those relative high values of Σ_{Nu} can be correlated with the mean value of $\langle Nu \rangle$ observed on the two last tubes presented on Figure 12a. In fact the value of $\langle Nu \rangle$ of the last tube rows for $Re_{2b} = 2,500$ are the highest values compared to the two first tube rows $\langle Nu \rangle$ values (unlike for the lower values of Re_{2b}). For comparison we can notice that for $Re_{2b} = 500$ between the first tube row and the last tube row there is an important decrease of about 50% whereas for $Re_{2b} = 2,500$ there is an increase of about 30%.

The comparison between Figure 12b and Figure 9 also shows that deviations of Nusselt numbers are globally in correlation with turbulent fluctuations suggesting that the row-by-row heat transfer fluctuations can be linked to the TKE budget. Thus, this analysis highlights how the unsteadiness and turbulence evolve according to the Reynolds number and the tube rows, and the correlation between the unsteadiness and the increase of the tubes heat exchange.

4. Conclusion

Numerical simulations have been carried out in a multi-rows elliptical finned-tube heat exchanger for four Reynolds numbers in the transitional regime by means of highly resolved Large Eddy Simulations. The evolution of the three-dimensional flow and its impact on heat transfer was studied throughout the heat exchanger (row by row). In a first part, a focus on a basic case (i.e the first row at the lower Reynolds number) has been presented in order to highlight the strong interactions between the flow topology including the horseshoe vortex system and the wall heat transfer, with a particular focus on the tubes.

In a second part, the influence of the tube row position of this four rows finned-tube heat exchanger was studied. It was found mainly that the topology of the near tube area counter-rotative vortices is highly dependent on the row considered. The variation of the counter-rotative vortices configurations leads to several upwash or downwash near wall flow configurations. Those

flow configurations lead to a clear variation on Nu distribution according to the row position. Thus it was possible to distinguish the flow configuration and heat transfer around the tubes rows into two parts i.e the two first rows and the two last rows.

In a third part, the influence of the Reynolds number was studied. The LES approach used in this study allowed analyzing how the transition to turbulence occurs within the heat exchanger as well as the unsteadiness and its impact on heat transfer. It was found that for the two lower Re_{2b} studied ($Re_{2b} = 500$ and $Re_{2b} = 1,000$), the unsteadiness was mainly located on the last tube row wake with Von Karman-like vortices developing outside downstream the heat exchanger. However when the Reynolds number increases the unsteadiness becomes very significant within the heat exchanger. Thus, for $Re_{2b} = 1,500$, more three-dimensional turbulent vortical structures appears in the vicinity of the last tube row, and for $Re_{2b} = 2,500$ the unsteadiness appears even more upstream with important turbulent vortical structures around the third tube row. Then it was found that the unsteadiness of the flow occurs sooner upstream from the trailing edge of the heat exchanger when the Reynolds number increases. Moreover regarding the tubes surface averaged Nu unsteadiness, for $Re_{2b} = 500$ no particular unsteadiness was observed even on the last tube. For $Re_{2b} = 1,000$ the unsteadiness was also very low but a slight increase of the unsteadiness was observed for the two last tube rows. For $Re_{2b} = 1,500$ and $Re_{2b} = 2,500$ a significant more important increase of the unsteadiness was found for the two last rows. This behaviour is shown to be in correlation with the TKE production determined by tube rows versus Reynolds Number. Finally an important increases of Nu value correlated with the vortical turbulent structures and unsteadiness was highlighted.

Further development would be to assess the performance of more simplified turbulence models such as unsteady-RANS models or even RANS model that are still used in evaluating the unsteadiness, and the laminar-turbulent transition. Are they correctly revealing the main vortical structures together with its interaction in those kind of heat exchanger.

Acknowledgments

The present work was supported by OSEO [grant contract number F1012001 R, OSEO] within the framework of a French joint programme: FUI-AAP10 Project CAFEE.

References

[1] L. Tian, Y. He, Y. Tao, W. Tao, A comparative study on the air-side performance of wavy fin-and-tube heat exchanger with punched delta winglets in staggered and in-line arrangements, International Journal of Thermal Sciences 48 (9) (2009) 1765 – 1776.

[2] Z. Wu, G. Ding, K. Wang, M. Fukaya, Application of a genetic algorithm to optimize the refrigerant circuit of fin-and-tube heat exchangers for maximum heat transfer or shortest tube, International Journal of Thermal Sciences 47 (8) (2008) 985 – 997.

[3] T. A. Tahseen, M. Ishak, M. Rahman, An overview on thermal and fluid flow characteristics in a plain plate finned and un-finned tube banks heat exchanger, Renewable and Sustainable Energy Reviews 43 (2015) 363 – 380.

[4] J. Herpe, D. Bougeard, S. Russeil, M. Stanciu Numerical investigation of local entropy production rate of a finned oval tube with vortex generators, International Journal of Thermal Sciences 48 (5) (2009) 922 – 935

[5] J. Simo Tala, D. Bougeard, S. Russeil, J.-L. Harion, Tube pattern effect on thermalhydraulic characteristics in a two-row finned-tube heat exchanger, International Journal of Thermal Sciences 60 (2012) 225 – 235.

[6] C. Baker, The laminar horseshoe vortex, Journal of Fluid Mechanics 95 (02) (1979) 347–367.

[7] B. Sahin, A. Akkoca, N. Öztürk, H. Akilli, Investigations of flow characteristics in a plate fin and tube heat exchanger model composed of single cylinder, International Journal of Heat and Fluid Flow 27 (3) (2006) 522 – 530.

[8] B. Sahin, A. Demir, Thermal performance analysis and optimum design parameters of heat exchanger having perforated pin fins, Energy Conversion and Management 49 (6) (2008) 1684 – 1695.

[9] J. Simo Tala, S. Russeil, D. Bougeard, J.-L. Harion, Investigation of the flow characteristics in a multirow finned-tube heat exchanger model by

means of PIV measurements, Experimental Thermal and Fluid Science 50 (2013) 45 – 53.

[10] D. Bougeard, Infrared thermography investigation of local heat transfer in a plate fin and two-tube rows assembly, International Journal of Heat and Fluid Flow 28 (5) (2007) 988 – 1002.

[11] D. Chatterjee, G. Biswas, S. Amiroudine, Numerical investigation of forced convection heat transfer in unsteady flow past a row of square cylinders, International Journal of Heat and Fluid Flow 30 (6) (2009) 1114 – 1128.

[12] L. Li, X. Du, Y. Zhang, L. Yang, Y. Yang, Numerical simulation on flow and heat transfer of fin-and-tube heat exchanger with longitudinal vortex generators, International Journal of Thermal Sciences 92 (2015) 85 – 96.

[13] L. Sun, C.-L. Zhang, Evaluation of elliptical finned-tube heat exchanger performance using CFD and response surface methodology, International Journal of Thermal Sciences 75 (2014) 45 – 53.

[14] G. Delibra, D. Borello, K. Hanjalić, F. Rispoli, URANS of flow and endwall heat transfer in a pinned passage relevant to gas-turbine blade cooling, International Journal of Heat and Fluid Flow 30 (3) (2009) 549 – 560

[15] K. Kritikos, C. Albanakis, D. Missirlis, Z. Vlahostergios, A. Goulas, P. Storm, Investigation of the thermal efficiency of a staggered elliptic-tube heat exchanger for aeroengine applications, Applied Thermal Engineering 30 (23) (2010) 134 – 142.

[16] G. Delibra, K. Hanjalić, D. Borello, F. Rispoli, Vortex structures and heat transfer in a wall-bounded pin matrix: LES with a RANS wall-treatment, International Journal of Heat and Fluid Flow 31 (5) (2010) 740 – 753

[17] J. Wen, D. Tang, Z. Wang, J. Zhang, Y. Li, Large eddy simulation of flow and heat transfer of the flat finned tube in direct air-cooled condensers, Applied Thermal Engineering 61 (2) (2013) 75–85.

[18] C. Baker, The turbulent horseshoe vortex, Journal of Wind Engineering and Industrial Aerodynamics 6 (12) (1980) 9 – 23.

[19] Y. Lai, M. Lu, Q. Wang, A large eddy simulation of plate-fin and tube heat exchangers with small diameter tubes, Heat Transfer Engineering 35 (11-12) (2014) 1137–1143.

[20] L.-Z. Zhang, W.-C. Zhong, J.-M. Chen, J.-R. Zhou, Fluid flow and heat transfer in plate-fin and tube heat exchangers in a transitional flow regime, Numerical Heat Transfer, Part A: Applications 60 (9) (2011) 766–784.

[21] S. A. N. Bordalo, F. E. M. A. Saboya, Pressure drop coefficients for elliptic and circular sections in one, two and three-row arrangements of plate fin and tube heat exchangers, Journal of the Brazilian Society of Mechanical Sciences 21 (1999) 600 – 610.

[22] J.-Y. Jang, J.-Y. Yang, Experimental and 3-d numerical analysis of the thermal-hydraulic characteristics of elliptic finned-tube heat exchangers, Heat Transfer Engineering 19 (4) (1998) 55–67.

[23] F. Nicoud, F. Ducros, Subgrid-scale stress modelling based on the square of the velocity gradient tensor, Flow, Turbulence and Combustion 62 (3) (1999) 183–200.

[24] C.-W. Lu, J.-M. Huang, W. Nien, C.-C. Wang, A numerical investigation of the geometric effects on the performance of plate finned-tube heat exchanger, Energy Conversion and Management 52 (3) (2011) 1638 – 1643.

[25] N. Jarrin, S. Benhamadouche, D. Laurence, R. Prosser, A synthetic-eddy-method for generating inflow conditions for large-eddy simulations, International Journal of Heat and Fluid Flow 27 (4) (2006) 585 – 593

[26] N. Gourdain, Prediction of the unsteady turbulent flow in an axial compressor stage. part 1: Comparison of unsteady RANS and LES with experiments, Computers & Fluids 106 (2015) 119 – 129.

[27] A. Colleoni, A. Toutant, G. Olalde, Simulation of an innovative internal design of a plate solar receiver: Comparison between RANS and LES results, Solar Energy 105 (2014) 732 – 741.

[28] O. Zikanov, Essential computational fluid dynamics, John Wiley & Sons, 2010.

[29] J. V. Simo Tala, S. Russeil, D. Bougeard, J.-L. Harion, Numerical analysis of the fin spacing effect on the horseshoe vortex system evolution in a two-row finned-tube heat exchanger, International Journal of Numerical Methods for Heat & Fluid Flow 23 (7) (2013) 1136–1154.

[30] U. Piomelli, E. Balaras, Wall-layer models for large-eddy simulations, Annual Review of Fluid Mechanics 34 (1) (2002) 349–374.

[31] O. Lehmkuhl, I. Rodríguez, A. Baez, A. Oliva, C. Pérez-Segarra, On the large-eddy simulations for the flow around aerodynamic profiles using unstructured grids, Computers & Fluids 84 (0) (2013) 176 – 189.

[32] R. D. Moser, J. Kim, N. N. Mansour, Direct numerical simulation of turbulent channel flow up to Re = 590, Physics of Fluids 11 (4) (1999) 943–945.

[33] W. A. A. Hunt, J. C. R., P. Moin, Eddies, stream, and convergence zones in turbulent flows, Center for Turbulence Research Report CTR-S88 (1988) pp. 193–208.

[34] E. Toubiana, S. Russeil, D. Bougeard, N. François, Large eddy simulation and Reynolds-Averaged Navier-Stokes modeling of flow in staggered plate arrays: Comparison at various flow regimes, Applied Thermal Engineering 89 (2015) 405 – 420.

[35] J. Jeong, F. Hussain, On the identification of a vortex, Journal of Fluid Mechanics 285 (1995) 69–94.

[36] R. Romero-Méndez, M. Sen, K. T. Yang, R. McClain, Effect of fin spacing on convection in a plate fin and tube heat exchanger, International Journal of Heat and Mass Transfer 43 (1) (2000) 39 – 51.

[37] S. Balabani, M. Yianneskis, Vortex shedding and turbulence scales in staggered tube bundle flows, The Canadian Journal of Chemical Engineering 75 (5) (1997) 823–831

[38] C. Liang, G. Papadakis Large eddy simulation of cross-flow through a staggered tube bundle at subcritical Reynolds number, Journal of Fluids and Structures 23 (8) (2007) 1215–1230

Table 1: Thermo-physical properties of the air and fin

	$C_p\ (J \cdot kg^{-1} \cdot K^{-1})$	$\lambda\ (W \cdot m^{-1} \cdot K^{-1})$	$\rho\ (kg \cdot m^{-3})$	$\mu\ (Pa \cdot s)$
Air	1003.62	0.026	$353.02/T$	$1.86 \cdot 10^{-5}$
Fin	903	237	2702	

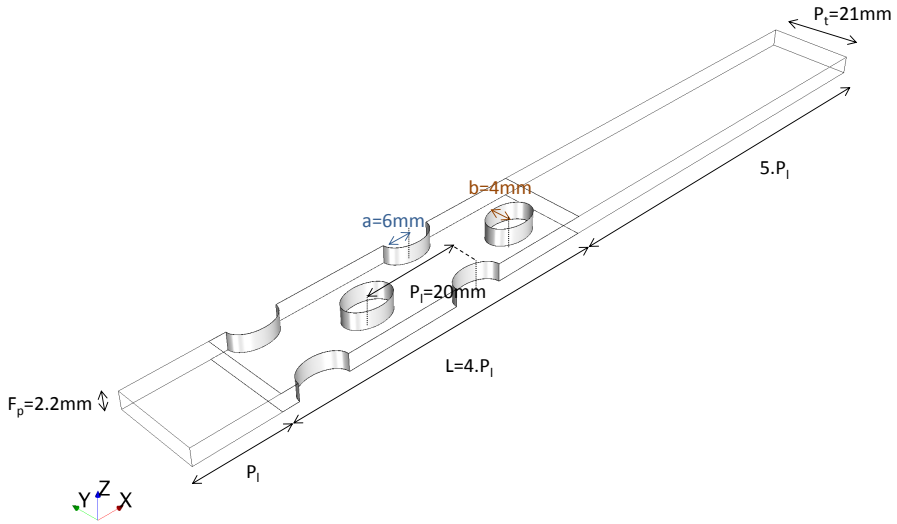

(a) Computational domain

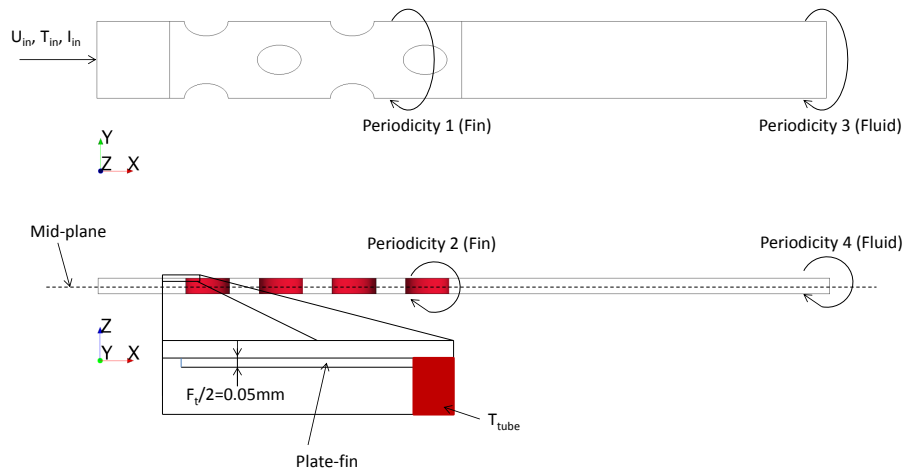

(b) Boundary conditions

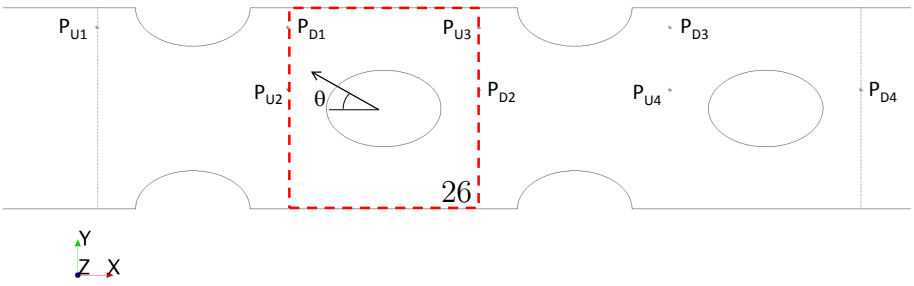

(c) Probes and tube row averaging-zone

Figure 1: Computational domain, boundary conditions and postprocessing features

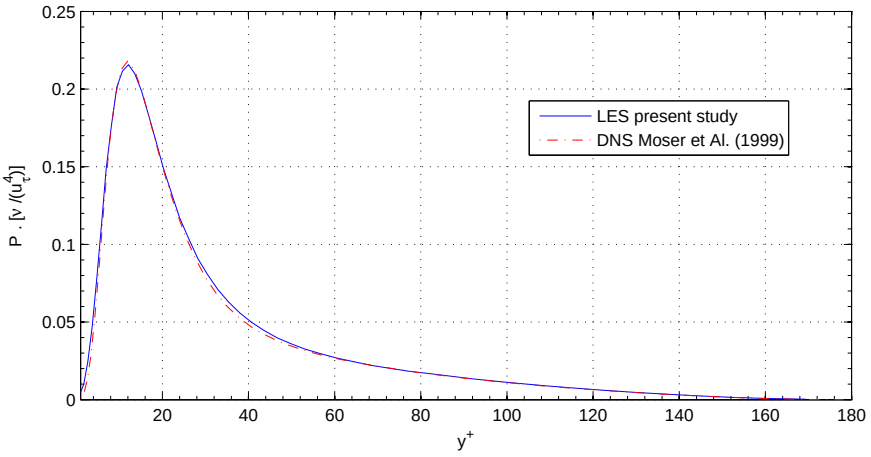

(a) Production of turbulent kinetic energy

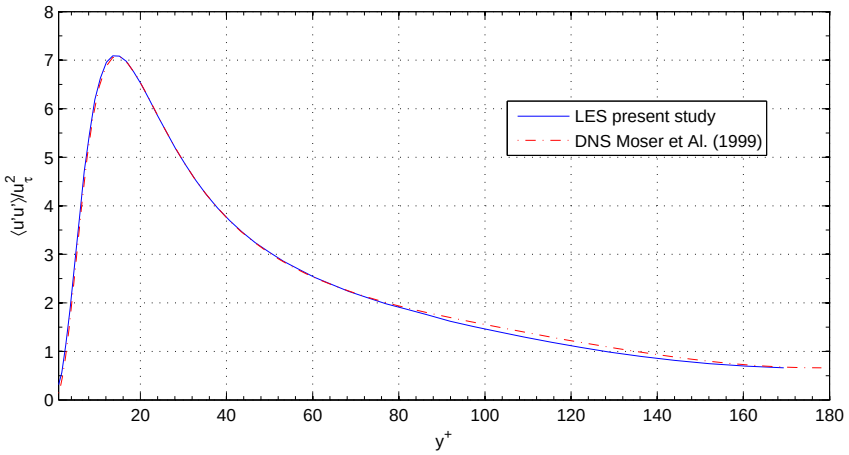

(b) R_{uu}

Figure 2: Comparison between LES calculation and DNS results for plate channel flow [32]

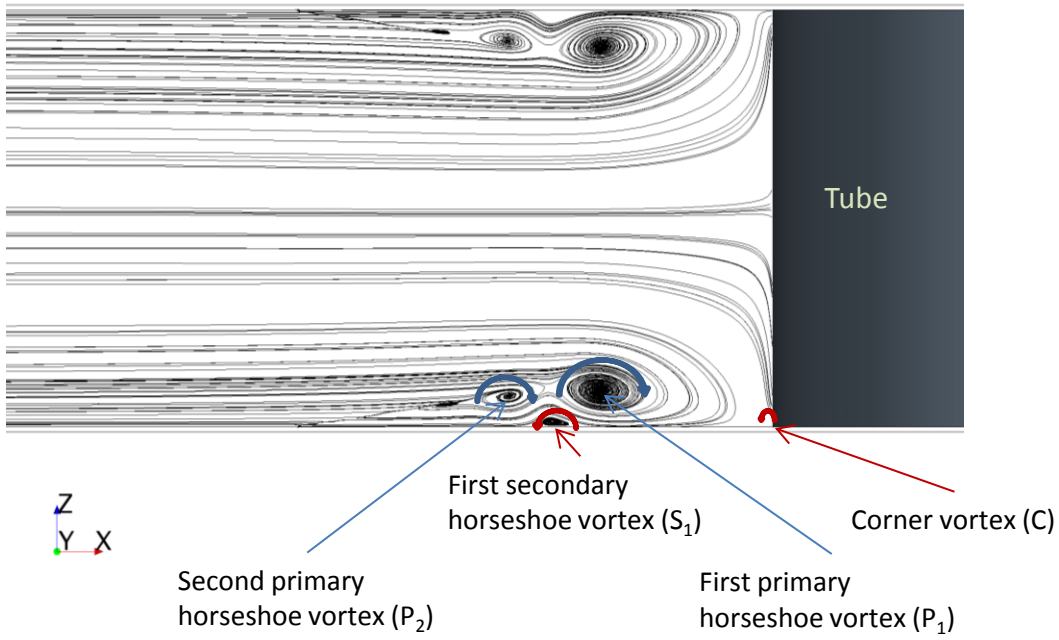

Figure 3: Illustration of a typical horseshoe vortex system upstream a tube-fin junction in the mid-plane of symmetry perpendicular to the fin (second tube row, $Re_{2b} = 1,500$)

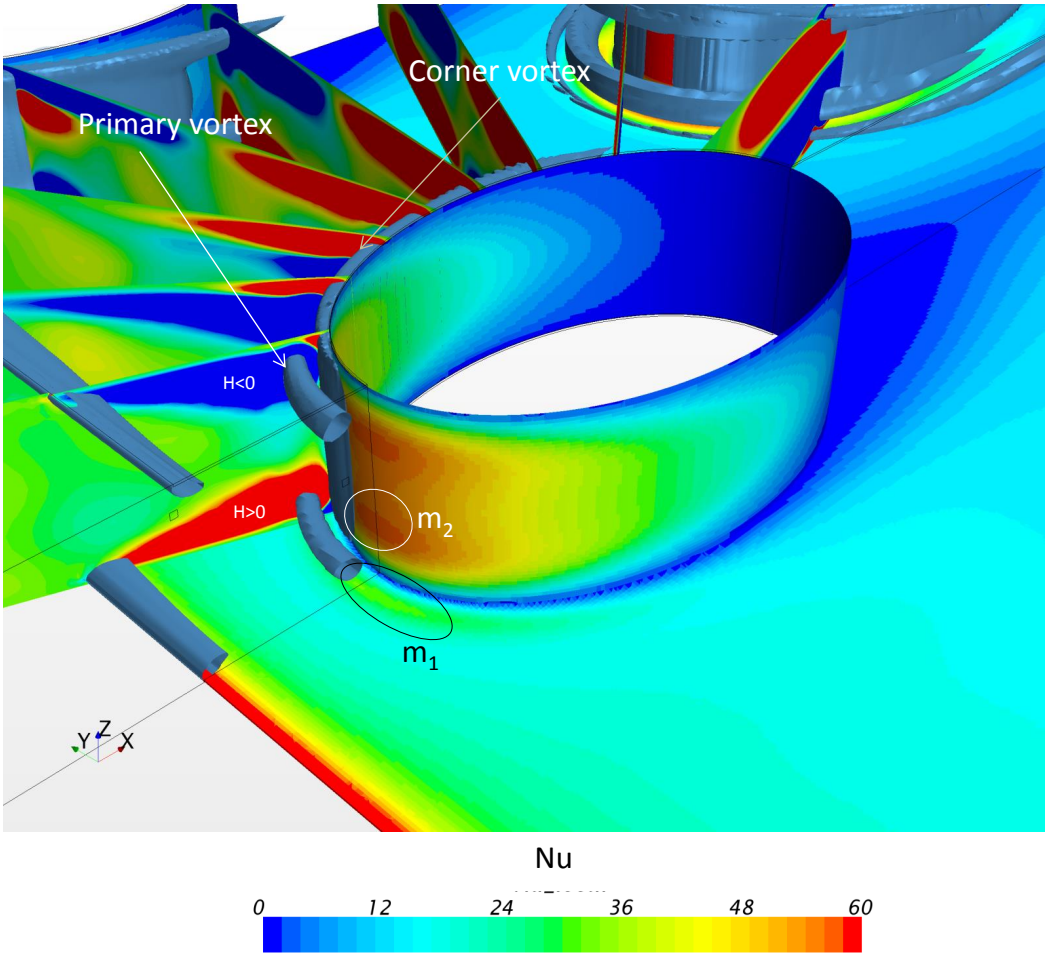

Figure 4: Illustration of the impact of horseshoe vortical structures on heat transfer, first row of the heat exchanger, $Re_{2b} = 500$

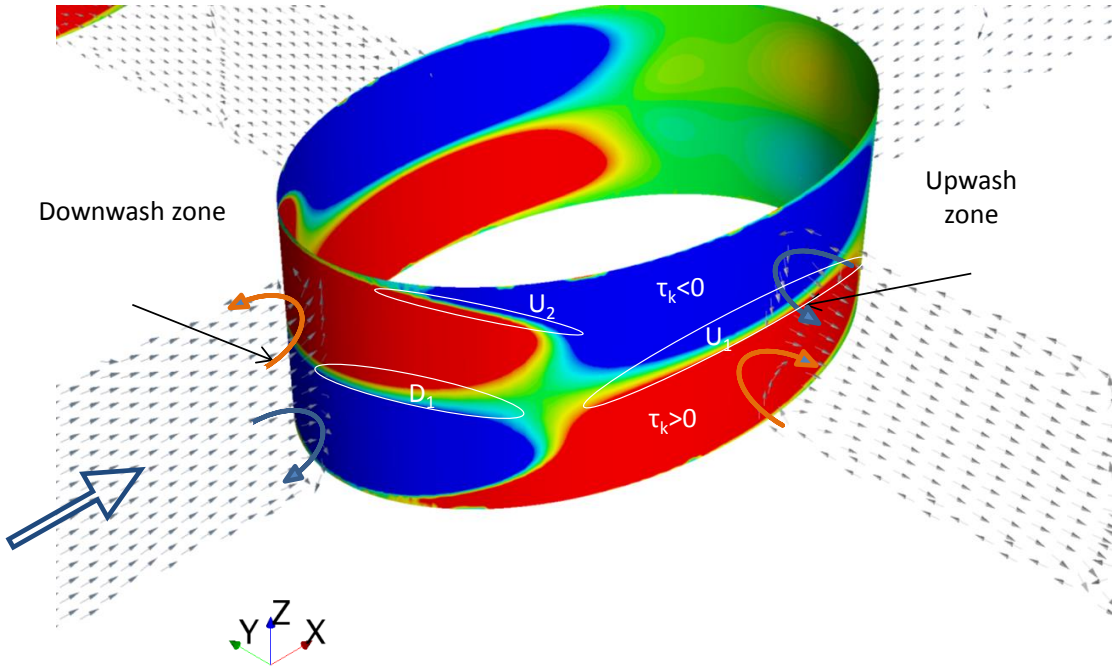

Figure 5: Distribution of the z-component of wall shear stress of the tube wall and tangential velocity vector distribution over two radial planes ($\theta = 0°$ and $\theta = 90°$)

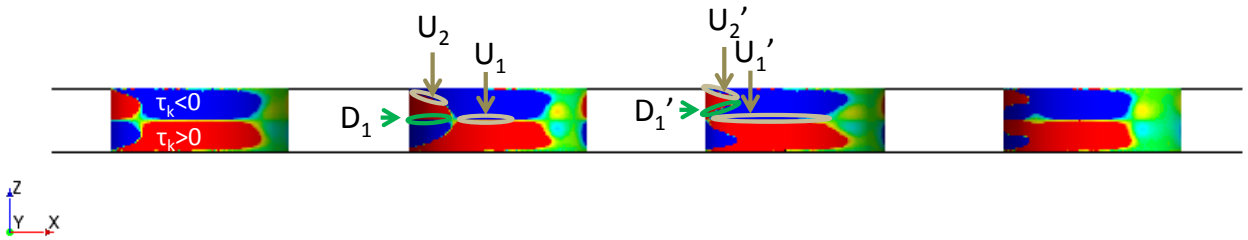

(a) $Re_{2b} = 500$

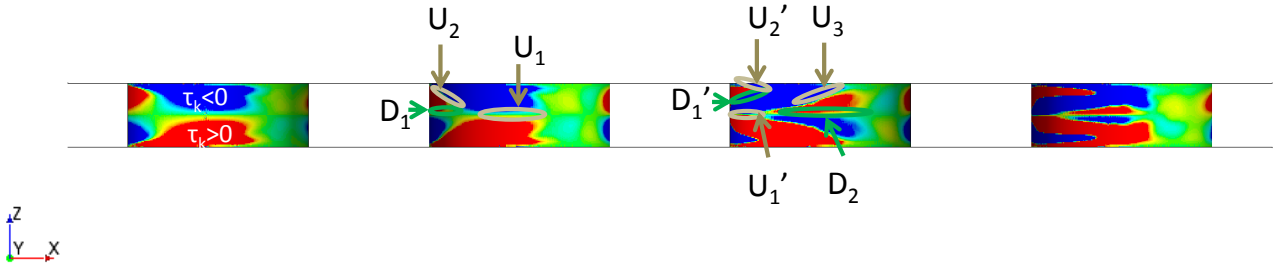

(b) $Re_{2b} = 1,500$

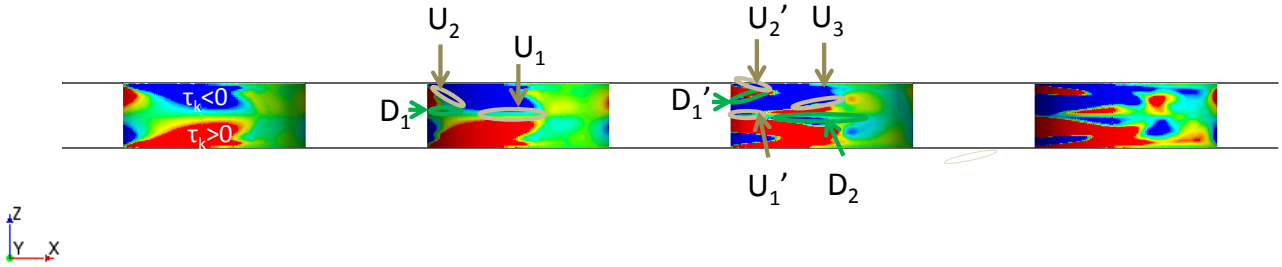

(c) $Re_{2b} = 2,500$

Figure 6: Wall shear stress ($\langle \tau_k \rangle$ component) distribution on tube wall for each row, side view, (incoming flow is from left to right)

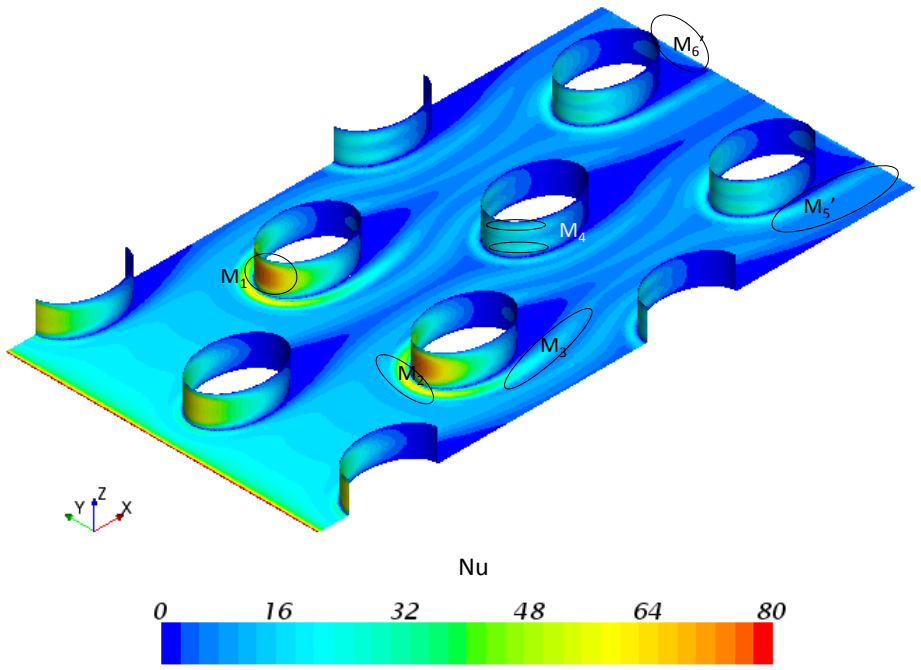

(a) $Re_{2b} = 500$

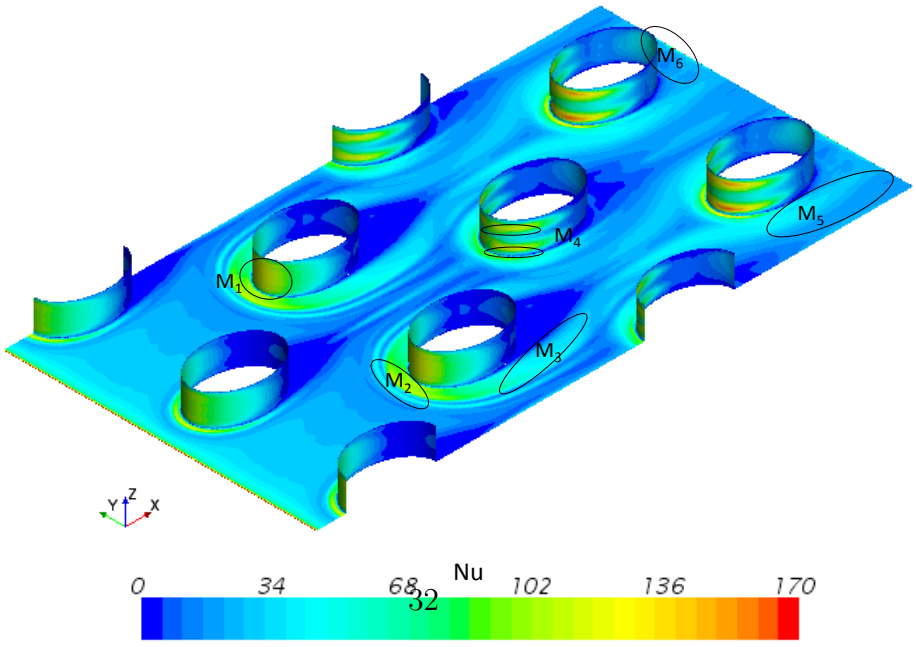

(b) $Re_{2b} = 2,500$

Figure 7: Local time-averaged Nu distribution on the heat exchanger walls (tubes an fin), for $Re_{2b} = 500$ and $Re_{2b} = 2,500$

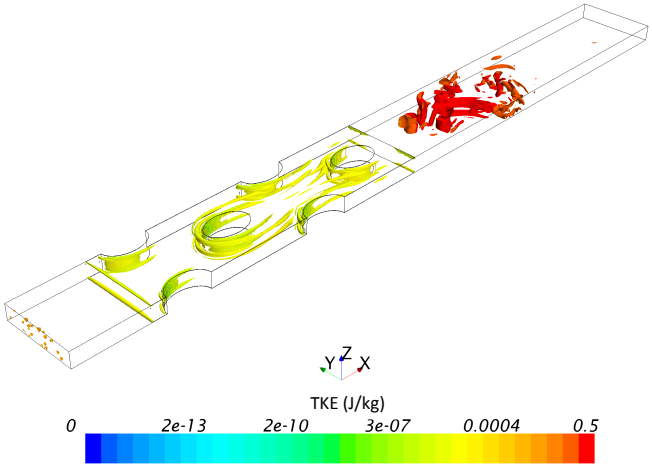

(a) $Re_{2b} = 500$

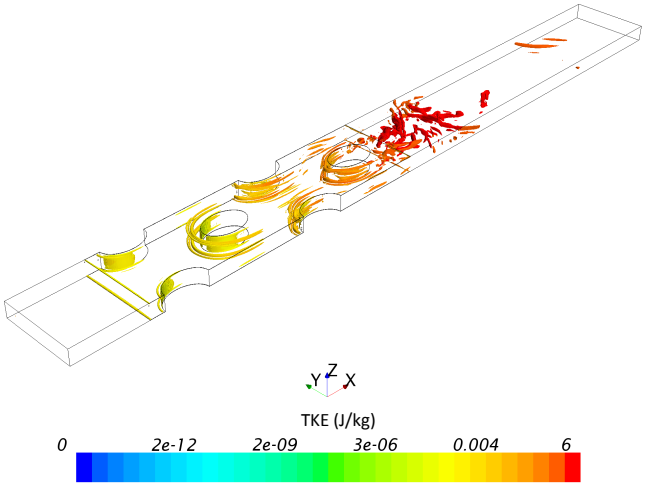

(b) $Re_{2b} = 1,500$

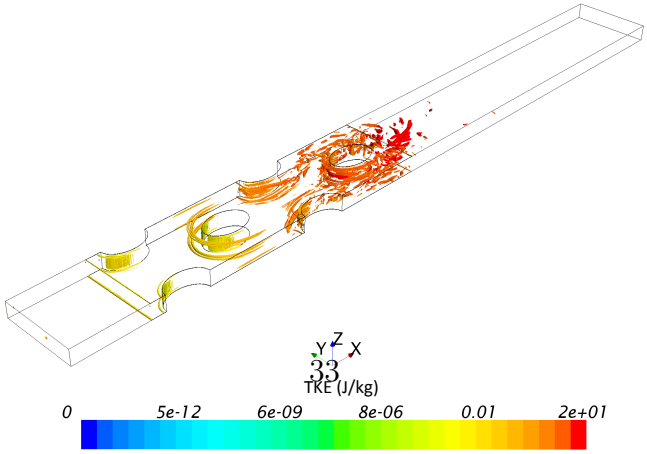

(c) $Re_{2b} = 2,500$

Figure 8: Instantaneous vortices identified by λ_2 vortex criterion

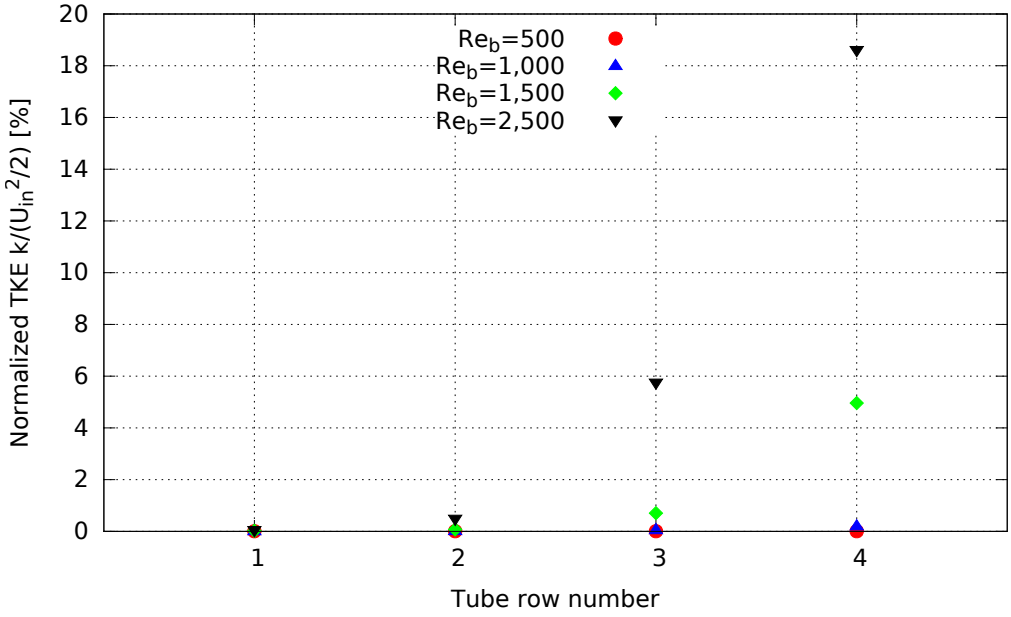

(a) Linear scale

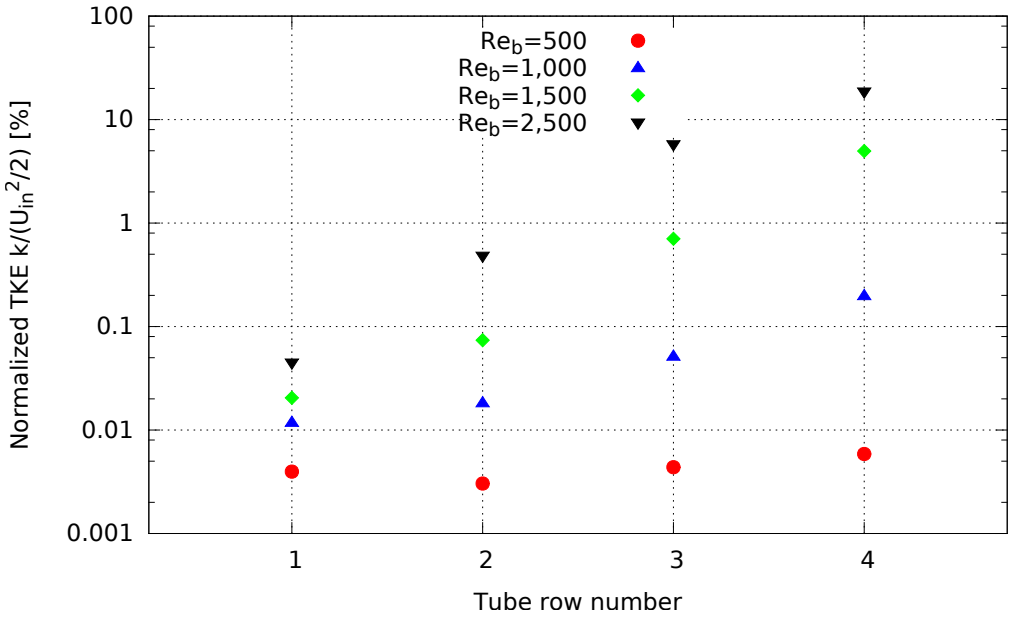

(b) Logarithmic scale

Figure 9: Normalized time averaged and volume-averaged turbulent kinetic energy

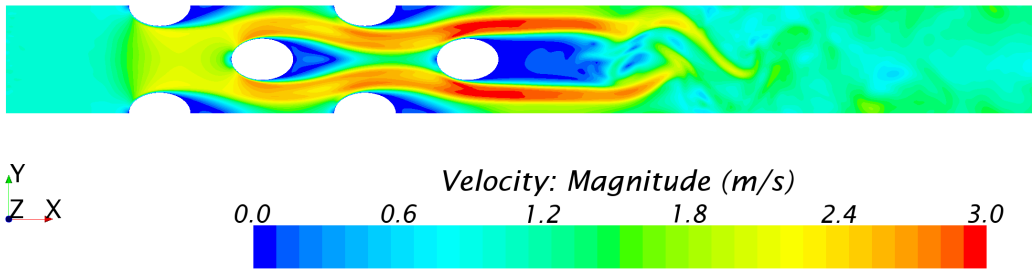

(a) $Re_{2b} = 500$

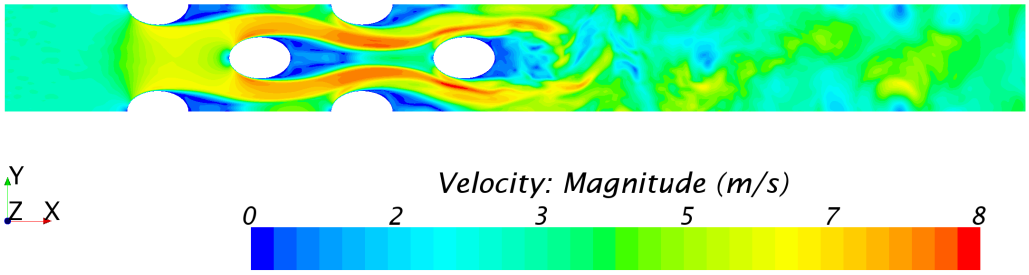

(b) $Re_{2b} = 1,500$

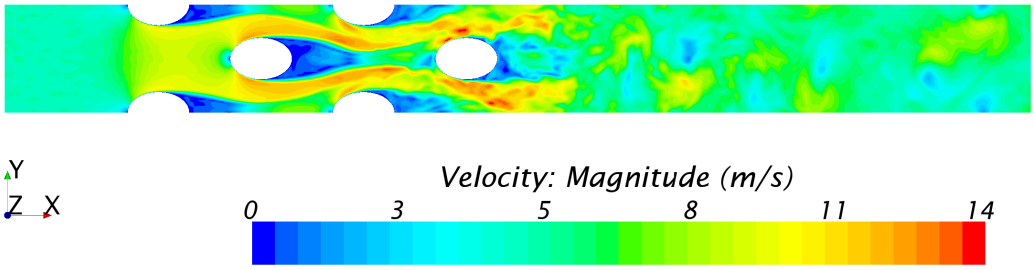

(c) $Re_{2b} = 2,500$

Figure 10: Instantaneous velocity magnitude in the midplane (50% of the tube height)

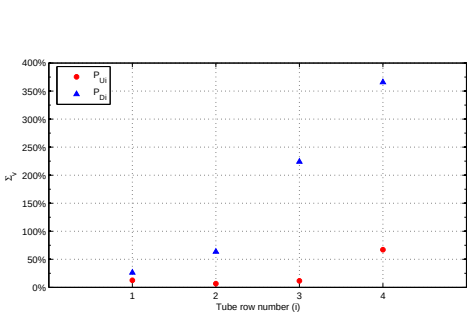

(a) Normalized standard deviation Σ_v values for probes temporal variation located upstream and downstream each tube

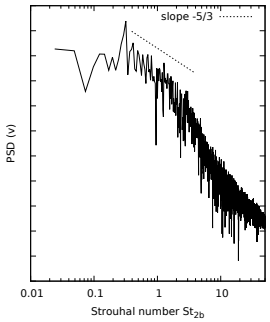

(b) Power spectral density of v at location P_{D4}

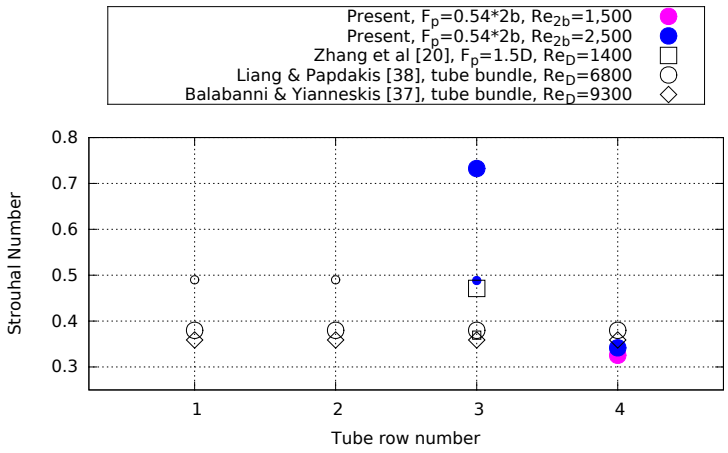

(c) Row-by-row distribution of Strouhal numbers ($St_{2b} = f2b/U_{in}$ or $St_D = fD/U_{in}$). Big and small items are primary and secondary frequencies respectively

Figure 11: Flow unsteadiness based on the analysis of the y-component velocity v for $Re_{2b} = 2,500$.

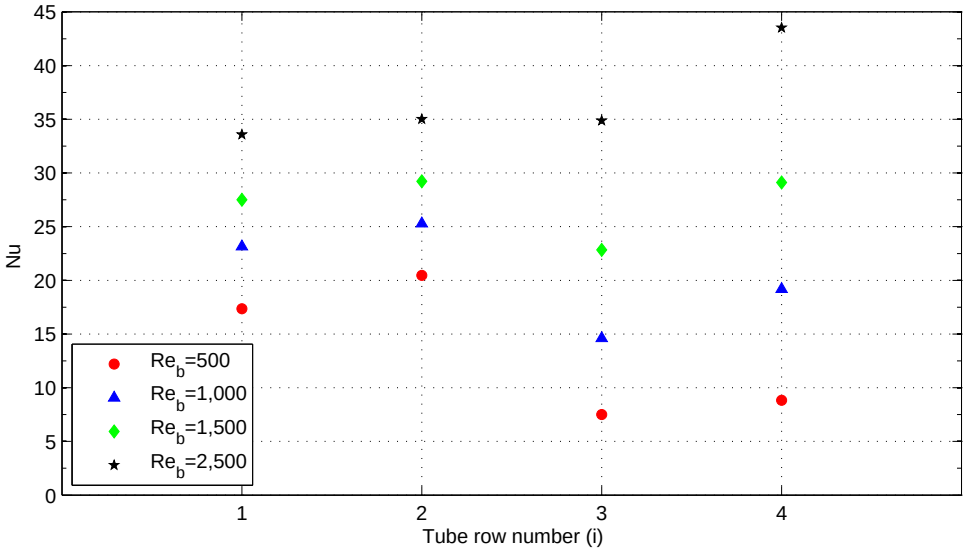

(a) Tube surface mean value of $\langle Nu \rangle$

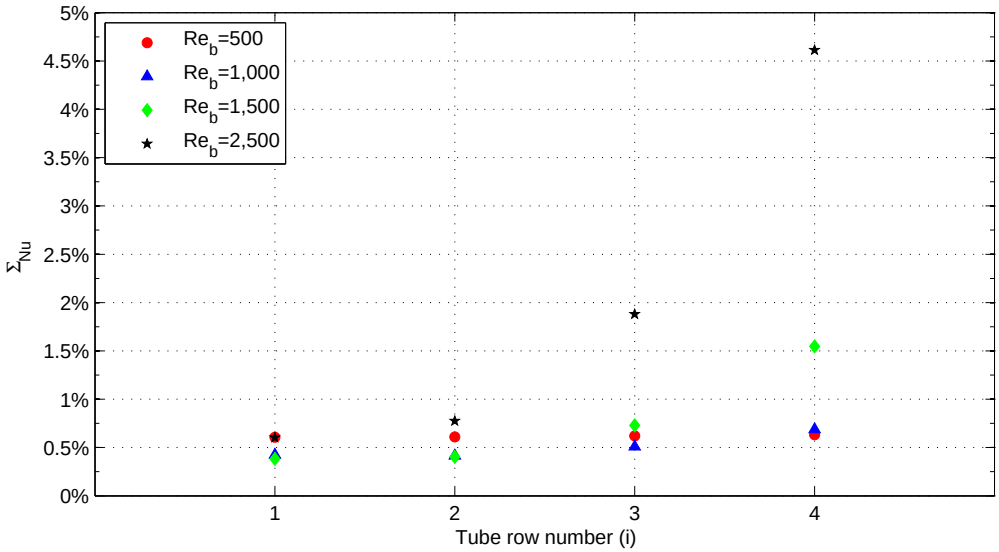

(b) Σ_{Nu}

Figure 12: Tube surface mean value of $\langle Nu \rangle$ and normalized standard deviation Σ_{Nu} values for surface mean value of Nu temporal variation